Sustainable Energy & Fuels

ROYAL SOCIETY OF CHEMISTRY

PAPER

View Article Online
View Journal | View Issue

Cite this: *Sustainable Energy Fuels*, 2026, **10**, 2327

Electrochemical conversion of CO_2 plasmas

Haytham E. M. Hussein, [ad] Panagiotis N. Kechagiopoulos [*b] and Angel Cuesta [*ac]

The integration of non-thermal CO_2 plasma (NTP) with a custom-designed electrolyte-gap electrolyser and CuO catalysts represents an innovative strategy to enhance the electrochemical conversion of CO_2 into C1–C3 products. Systematic galvanostatic experiments conducted at current densities ranging from 100 to 225 mA cm^{-2} demonstrated that plasma-on operation significantly reduces cell voltages (by up to ~1.3 V) and that product selectivity transitions from C1 species (CO and methane) to C2+ products, including ethylene, ethanol, acetate, propylene, and propanol. While CO and H_2 predominate under plasma-off conditions, with limited formation of C2 products, the hybrid plasma–electrochemical system increases the faradaic efficiency (FE) for ethylene up to 39.5% and ethanol up to 18.1%. These enhancements are attributed to plasma-generated reactive species (radicals and excited-state molecules) that lower kinetic barriers for C–C coupling and modify the interfacial pH, thereby reducing parasitic carbonate/bicarbonate losses. The plasma-on state resulted in a statistically significant increase in liquid product carbon efficiency, from an average of ~0.41% during plasma-off experiments to ~0.91% during plasma-on experiments. Although the system currently exhibits lower overall energy efficiency owing to the power demands of the plasma discharge, this work establishes a robust framework for flexible product tuning and sustainable carbon utilisation *via* plasma-activated feeds.

Received 10th November 2025
Accepted 2nd April 2026

DOI: 10.1039/d5se01488c

rsc.li/sustainable-energy

Introduction

The electrochemical conversion of CO_2 into value-added chemicals and fuels—specifically C2 and C3 products—and their scalability can aid efforts to decelerate climate change and produce chemicals from sources alternative to crude oil and gases.[1] Many studies have explored the electrocatalytic conversion of CO_2, emphasising the importance of transition metal surfaces such as Cu in converting CO_2 into valuable chemicals such as methane, ethylene, and ethanol.[2–5]

Lab-scale electrochemical CO_2 conversion typically uses flow cells with either an electrolyte-gap-membrane electrode assembly (MEA) or a zero-gap MEA,[6–9] because gas diffusion electrodes (GDEs) allow overcoming the low solubility of CO_2 in the most commonly used solvent, water. Research focuses on developing and optimising the catalyst,[10–12] the electrolyte composition,[13–15] the pH,[16–20] the operating temperature,[21] and the polymer-electrolyte membrane in the MEA.[22]

For instance, Gonçalves *et al.*[23] demonstrated the selective production of C2 hydrocarbons, particularly ethylene, using copper electrodes modified *via* electroplating. Gao *et al.*[24] investigated the effect of designing and modifying electrocatalyst structures, the influence of electrolytes on selectivity and conversion rate, and the potential applications of electrolysers for large-scale CO production. Other studies have explored the possible integration of CO_2 conversion processes with renewable energy sources, such as the work by Kauffman *et al.*[25] to increase reaction rates and product selectivity.

Cu and Cu-based materials are the most common catalysts capable of electrocatalytically reducing CO_2 beyond C1 products, such as CO/HCOOH/C_2H_4, with significant faradaic efficiency (FE).[26,27] This functional property stems from Cu's ability to activate C–C coupling through CO adsorption.[28] Nonetheless, electrochemical CO_2 conversion using Cu often requires high overpotentials to achieve a reasonable reaction rate and selectivity towards C2+ products, limiting the practical applications of Cu catalysts.[29] Furthermore, applying high current densities or high overpotentials leads to the detachment of the catalysts or rapid deactivation, in addition to competition with the hydrogen evolution reaction (HER).[29–31]

Several mechanisms have been proposed to explain the production of C2+ products at the Cu surface. Surface oxygen species and electrophilic $Cu^{\delta+}$ species with low coordination in oxide-derived materials are assumed to play a critical role in the activity and selectivity for C2+ production.[32] Research work has suggested that Cu^+/Cu^0 surface species promote CO_2 conversion

[a]*Advanced Centre for Energy and Sustainability (ACES), School of Natural and Computing Sciences, University of Aberdeen, Aberdeen, Scotland AB24 3UE, UK. E-mail: angel.cuestaciscar@abdn.ac.uk; acuesta@iqf.csic.es*

[b]*Chemical Processes & Materials Group, School of Engineering, University of Aberdeen, Aberdeen AB24 3UE, UK. E-mail: p.kechagiopoulos@abdn.ac.uk*

[c]*Instituto de Química Física Blas Cabrera, CSIC, C. Serrano 119, E-28006 Madrid, Spain*

[d]*GSK Carbon Neutral Laboratories for Sustainable Chemistry, Jubilee Campus, University of Nottingham, Wollaton Road, Nottingham, NG8 1BB, UK*

to C2+ products due to an enhanced ability for CO_2 activation and C–C coupling.[24,33] On the other hand, recent studies have focused on controlling the local surface electronic structure by combining surface Cu with other metal atoms in atomic proximity,[34,35] to promote C–C coupling on asymmetric atom pairs, thus accelerating C2+ production by CO dimerisation.[34,35] However, bimetallic systems such as CuAg, CuPd, and CuAu promote forming C1 products over C2 products, and show poor selectivity.[34,35] Furthermore, production of C3 terminal oxygenates (*e.g.*, propanol) and hydrocarbons (*e.g.*, propylene) has been reported in only a few studies, with reaction mechanisms that are controlled by the presence of specific intermediates such as $*OCH_2CH_3$ or the coupling between adsorbed/molecular carbon dioxide or carboxyl with the $*C_2$ intermediates that are involved in the ethylene pathway.[13,36]

One of the key advantages of electrochemical CO_2 conversion is its flexibility in adjusting the product distribution and its potential for modular design. This adaptability allows us to tailor reactor designs for specific applications, making it an attractive option for carbon-intensive manufacturing industries seeking to use renewable energy for CO_2 conversion. Hence, to improve reactor engineering for CO_2 electrochemical reduction, research has focused on managing the reactants and flow cell architectures. However, CO_2 is a thermodynamically stable molecule, making its conversion into chemicals or fuels an energy-intensive process. Recently, a combination of electrochemical reactions with a non-thermal plasma (NTP) has been used to convert N_2 into ammonia.[37] Similarly, the hybridisation of a dielectric barrier discharge and a solid oxide electrolyser cell has been used to convert CO_2.[38] NTPs generate energetic electrons that activate small molecules, such as CO_2 and N_2, under ambient conditions, and subsequent electrocatalysis enables the selective formation of products under mild conditions. Combining both approaches may enhance the conversion efficiency, selectivity, and energy utilisation. For instance, in the work by Kumari *et al.*,[37] the plasma-assisted electrochemical system produced 47% more ammonia than the sum of the plasma-only and electrochemical-only conditions. In this work, we investigated the impact of the nature of the CO_2 feed on the conversion activity and selectivity for producing C2+ by engineering a lab-scale reactor that can be fed with either CO_2 or a CO_2 NTP at the cathode. Our research revealed that plasma activated CO_2 species, including vibrationally excited CO_2 molecules and neutral and ionic radicals, play a role in enhancing the electrochemical conversion of CO_2 into C2+ gas and liquid products. By addressing these key areas, we aim to develop reactor architectures and system engineering strategies that will enable further advancements in CO_2 conversion technology and inspire potential industrial applications.

Experimental

Chemicals

Cesium hydrogen carbonate, 99.99%, ($CsHCO_3$, Thermo Scientific Chemicals), cesium methanesulfonate, 98%, ($Cs(SO_3CH_3)$, Thermo Scientific Chemicals), and cesium sulfate, 99+%, pure, (Cs_2SO_4, Thermo Scientific Chemicals) were used to prepare the electrolyte. The electrolyte composition was 0.5 M $CsHCO_3$ + 0.25 M $Cs(SO_3CH_3)$ + 0.25 M Cs_2SO_4 in water. The choice of Cs^+ is consistent with cation-size-driven field effects that stabilise dipolar intermediates on Cu and can promote multi-carbon products.[1,39–41] In addition, this mixture of salts minimises the formation of carbonate and bicarbonate during the electrochemical reduction of CO_2.[14,42] Note that while alkali metal cations are traditionally viewed as chemically inert, their hydration shells undergo significant polarisation within the high-strength electric field of the electrical double layer (EDL).[42,43] Although the bulk pK_a of hydrated Cs^+ is approximately 14.7, the intense interfacial field effectively lowers this value at the electrode surface.[44] This allows larger cations to mitigate the accumulation of OH^- generated during reduction.[45–47] By maintaining the interfacial pH within a range that favours molecular CO_2 stability (typically <9–10), this buffering effect prevents the competitive shift toward non-reducible carbonate species:[48]

$$CO_2 + 2OH^- \rightarrow CO_3^{2-} + H_2O.$$

The choice of methanesulfonate ($CH_3SO_3^-$) as a spectator electrolyte is supported by its high cathodic stability compared to the targeted CO_2RR and the competing hydrogen evolution reaction (HER).[46,49] The reductive cleavage of the methanesulfonate C–S bond occurs at significantly more negative potentials (approximately −1.5 V *vs.* RHE), ensuring that the anion remains intact. Unlike halides, the "hard" nature of the sulfonate group results in negligible specific adsorption, preserving the catalyst's active sites for CO_2 intermediates (*COOH, *CO).[49]

Cupric oxide (CuO, 99.9%) and iridium(IV) oxide (IrO_2, 99.9%) nanoparticle catalysts were purchased from Sigma Aldrich. All aqueous electrolytes used in this study were prepared using 18 MΩ cm water (Thermo, smart2pure). All chemicals were used as received without further purification.

Preparation of the electrodes and membranes

The cathodes were fabricated by spraying the catalyst ink onto the gas diffusion layer (GDL; Fuelcellstore, Sigracet 39 BB, a non-woven carbon paper microporous layer (MPL) that had been treated with PTFE to 5 wt%). The catalyst ink was prepared by suspending 30 mg of commercial CuO nanoparticles in a mixture of 500 μL of isopropanol and 200 μL of water. The catalyst ink was then stirred overnight to ensure uniform mixing and sprayed onto Sigracet 39 BB at room temperature using a Neo for Iwata TRN1 gravity feed airbrush. A similar procedure was used to prepare the anode; however, CT carbon cloth was used with MPL (Fuelcellstore) as the GDL instead of Sigracet 39 BB, and IrO_2 was used as the catalyst. The anode catalyst ink was also modified by adding 1 μL of a binder solution of 5% PTFE dissolved in isopropanol. A piperION® Anion Exchange Membrane (AEM; Fuelcellstore), 20 μm thick, self-supporting, was used as the membrane separating the anode and cathode. The AEM was immersed in 1 M $CsHCO_3$ for 48 h and then washed with deionised water several times before use in the

electrolyser. Scanning electron microscopy (SEM) images and energy-dispersive X-ray spectroscopy (XEDS) data of the anode and cathode are shown in Fig. S1.

Electrolysers

The electrolyte gap electrolyser was custom-made using a flow cell setup, as illustrated in Fig. 1 and S2. A 3 mm thick catholyte flow field compartment (3D printed, Tough 2000 Resin, Formlabs) was placed between the cathode gas diffusion electrode (GDE) and the AEM (Fig. 1 and S2). A 3 mm-thick gas flow field was introduced between a rigid 3D-printed PEEK plate (identified as a gas chamber in Fig. 1 and S2, 8 mm thick, Rigid 10 K Resin, Formlabs) and the cathode GDE. The gas flow field and chamber fed the reactant, either CO_2 gas or CO_2 NTP, to the cathode. The anolyte and catholyte comprised the same electrolyte solution, consisting of 0.5 M $CsHCO_3$, 0.25 M $Cs(SO_3CH_3)$, and 0.25 M Cs_2SO_4 in water, and were circulated to the anode and cathode, respectively. The cathode GDE, which is sandwiched between two gaskets, separates the catholyte flow field from the cathode CO_2 gas/CO_2 NTP chamber. The CuO catalyst layer faces the catholyte compartment, whereas the CO_2 gas/CO_2 NTP flows on the opposite side of the PTFE-treated MPL/GDL.

Carbonate/bicarbonate quantification was performed *ex situ* using electrolyte samples collected from the outlet streams during galvanostatic operation. Samples were collected over defined time windows, sealed to minimise CO_2 exchange with air, and analysed by two-step acid titration (first endpoint ~pH 8.3; second endpoint ~pH 4.5).

The geometric area of the cathode, which was used to calculate the current density, was 1 cm^2. CO_2 (99.999%, BOC) was fed to the cathode, and a 1 M solution of mixed Cs (the electrolyte) was flowed to both the cathode and anode. The gas products were analysed using a gas chromatograph (GC, Thermo Scientific, Trace1300) equipped with a thermal conductivity detector (TCD) and a ShinCarbon ST micropacked column (100/120, 2 m, 1 mm ID). Ultra-high-purity He (99.9999%, BOC) or high-purity N_2 (99.99%) was used as the

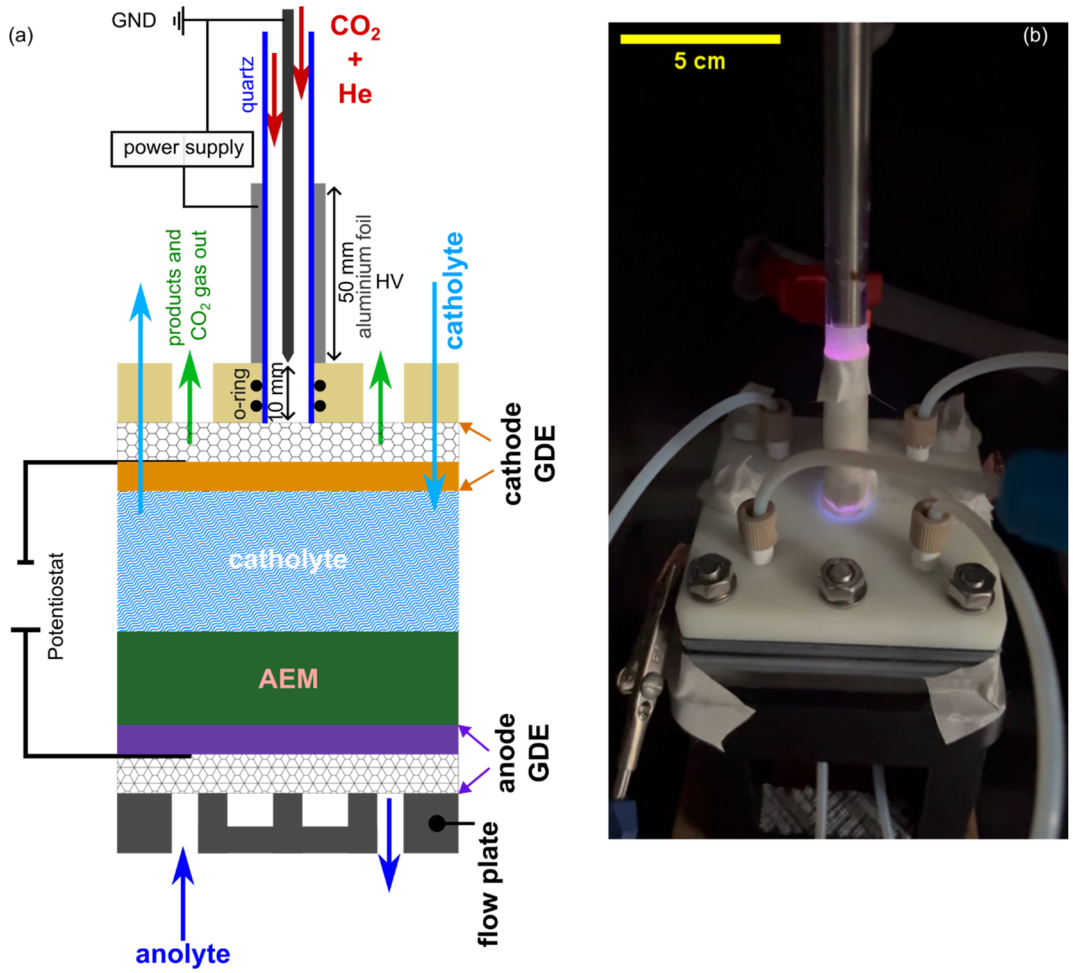

Fig. 1 (a) A schematic representation of the electrolyte-gap electrolyser showing the interface between the CO_2 NTP DBD and the cathode GDE. (i) Quartz tube (7 mm ID/9 mm OD) with coaxial DBD electrodes (internal grounded stainless-steel rod; external HV foil), (ii) 50 mm long HV foil, axially positioned 10–60 mm upstream of tube exit, (iii) the exit plane of the glass tube is levelled with the bottom side of the housing plate, the plasma input was secured and sealed gas-tight by compressing two Viton O-rings and (iv) the distance from the grounded rod tip to the cathode surface is 10 mm. (b) Photograph of the experimental set-up showing the plasma ignition during the CO_2 conversion experiments.

carrier gas. The TCD detected H_2 using N_2 as the carrier and carbon-containing products (unreacted CO_2, CO, CH_4, C_2H_4, C_2H_6, and C_3H_6) using He as the carrier. A trap jar filled with cold water was installed after the cell output channel to examine the liquid products. The anolyte, catholyte, and water in the water trap were syringed out and analysed using ultra-high-performance liquid chromatography (UHPLC, UltiMate3000, Thermo Scientific) equipped with a refractive index, variable wavelength detector, and HyperREZ™ XP carbohydrate H+ LC Column. Electrochemical control was achieved using a Parstat MC potentiostat (Princeton Applied Research, Ametek SI).

CO_2 plasma experiments

A dielectric barrier discharge (DBD) non-thermal plasma (NTP) was generated using a coaxial electrode configuration inside a quartz tube (inner diameter: 7 mm; outer diameter: 9 mm). A 6.35 mm diameter stainless-steel rod placed along the tube axis served as the grounded electrode, while an aluminium foil wrapped around the outer wall of the quartz tube served as the high-voltage (HV) electrode. The HV foil length was 50 mm, and it was positioned axially 10–60 mm upstream of the tube exit plane (*i.e.* the downstream foil edge was 10 mm upstream of the tube exit). The DBD reactor was interfaced with the electrochemical CO_2 flow cell by inserting the quartz tube through a 3D-printed plate on the back of the cathode side of the electrolyser as shown in Fig. 1 and S2. The desired gases (CO_2 and He) flowed through the quartz tube at flow rates determined by Mass Flow Controllers (MFC) from Sensirion (SFC5500) and MKS (1179A). The plasma was driven by a high-voltage AC power supply (PVM500-2500) operating at a sinusoidal waveform of ~40 kHz. The voltage and charge were sampled using an HV probe (Cal Test CT4028) and a passive probe (Teledyne LeCroy PP020) that measured the voltage across a 9.671 nF ceramic capacitor connected to the ground line, respectively. Both probes were connected to a 100 MHz digital oscilloscope (B&K Precision 2194). All reported plasma measurements were performed at an applied power of 10 ± 0.5 W, estimated from the voltage and charge data by integrating the *Q–V* Lissajous plot (see Fig. S3 and S4). The DBD reactor was interfaced with the electrochemical CO_2 flow cell by inserting the quartz tube through a 3D-printed plate on the back of the cathode side of the electrolyser, with a hole that fits the 9 mm outer diameter of the quartz tube. The plasma input into the cathode was secured and sealed gas-tight using compression of two Viton O-rings. The distance from the internal DBD electrode's tip to the cathode's surface was 10 mm. To ensure safe operation, the external high-voltage (HV) foil electrode and its electrical connection were fully insulated using a silicone sleeve, and 3 M Scotch Cloth Tape with a glass finish, applied to cover the aluminium foil. The integrated plasma–electrolyser assembly was enclosed within a non-conductive polycarbonate housing. The internal surfaces of the housing were coated with an electromagnetic interference (EMI) shielding spray and grounded to mitigate external electromagnetic interference. The HV power supply was equipped with a hardware enable/disable switch, and a single-point grounding scheme was implemented to prevent unintended returns. The maximum applied voltage is 12 kV peak-to-peak (pk-pk), although the maximum possible voltage is 30 kV pk-pk. The flow rates were regulated by mass flow controllers, with CO_2 flow at 30 NmL min^{-1} and He flow at 5 NmL min^{-1}, resulting in a total flow of 35 NmL min^{-1}. Given the inner diameter of the quartz tube, which measures 7 mm, this configuration corresponds to a nominal average linear velocity of approximately 1.52 cm s^{-1} within the tube under standard conditions (ideal gas). Considering the coaxial configuration, with a 7 mm inner diameter tube and a 6.35 mm rod, the annular cross-sectional area is calculated to be 6.8×10^{-6} m^2. This configuration yields a nominal annular gas velocity of approximately 8.6 cm s^{-1}.

Experiment for preheating the CO_2 feed

In experiments focused on thermal control, the CO_2 feed was elevated to a temperature of 150 °C using an Omega heating tape (1.245 kW, 240 VAC, $1'' \times 8''$) installed upstream of the electrolyser. The temperature was controlled by a PID controller, and a K-type thermocouple, positioned just before the cathode gas inlet, was used to monitor the gas temperature. To prevent heat loss before the gas entered the cell, the heated gas line was insulated. This setup was used to evaluate whether the selectivity and voltage fluctuations observed during plasma-on operation were solely due to the increased temperature of the reactants.

Physical and chemical characterisation

Scanning electron microscopy (SEM) and energy-dispersive X-ray spectroscopy (XEDS) were performed using a Zeiss microscope at an operating voltage of 10 kV to image the morphology of the electrodes and at 15 kV to analyse the chemical composition of the catalysts before and after the experiments. Optical emission spectroscopy (OES) was used to identify the active species in the CO_2 plasma, as shown in Fig. S5, and Table S1. OES was conducted using an Avantes 5-Channel ULS4096CL-EVO AvaSpec rackmount spectrometer, with each channel specified independently to achieve a resolution of 0.1 nm across a broad wavelength range of 190 to 900 nm (grating of 1800 lines per mm for 190–350 nm, 349–500 nm, 499–643 nm, 642–733 nm, and 1200 lines per mm for 732–905 nm). Emission was collected under conditions equivalent to the experimental conditions using a five-furcated cable comprising five ×200 μm optical fibres, positioned inside the reactor tube downstream of the discharge. Spectra were acquired with an integration time of 30 s and averaged over three scans with dark-background subtraction applied. Wavelength calibration was performed using a calibration source (Mercury–Argon lamp).

Results and discussion

An AC power source was employed to generate CO_2 NTP. The gas feed through the DBD tube comprised CO_2 at a flow rate of 30 NmL min^{-1} combined with He at 5 NmL min^{-1}. In the plasma-off experiments, the cathode feed composition remained identical; however, the AC power supply was deactivated. In this context, "plasma-off" denotes conventional electrochemical CO_2 reduction (eCO_2) using molecular gas, whereas "plasma-

on" refers to the electrolysis of the CO_2 NTP effluent. Given that the cathode is positioned downstream of the DBD discharge region, with the grounded rod tip situated 10 mm from the cathode (that is, the GDE plane), the catalyst is primarily exposed to post-discharge (afterglow) species emanating from the quartz tube rather than the high-field microdischarge region.[37] Consequently, the flux and lifetime of activated neutrals, such as vibrationally excited CO_2/CO and radical species, during their transport from the discharge to the GDE, are critical in determining plasma–electrode coupling.[50–55] Furthermore, the current design allows for the flow to expand across the entire area of the GDE, thereby preventing localised concentration gradients. Initially, upon NTP ignition and without operating the electrochemical cell to facilitate CO_2 conversion into fuel, we observed the typical products of the CO_2 NTP,[50,56,57] specifically CO_2, CO, and oxygen, Fig. S6. We then recorded the cell voltage under zero net current conditions to study the electrical coupling control. As depicted in Fig. S7, electrical coupling control was performed before galvanostatic electrolysis, with the plasma being alternately activated and deactivated (10 min on and 10 min off) while the cell voltage *vs.* time (potentiostat log) was recorded. The trace was scrutinised for any synchronous modulation associated with the ~40 kHz high-voltage (HV) waveform.

Electrocatalytic performance and product selectivity transitions

The electrocatalytic activity was initially evaluated by collecting linear sweep voltammograms (LSV) at 50 mV s^{-1} under plasma-on and off conditions, as shown in Fig. 2(a). The LSV (red curve) recorded under plasma-off conditions shows no cathodic peak, and the cathodic current begins to increase at a voltage more negative than −0.7 V *vs.* RHE due to CO_2 electrochemical reduction and HER, with the current rapidly rising above −0.8 V *vs.* RHE. In contrast, during plasma-on (CO_2 NTP DBD) experiments, the LSV (black curve) displayed a cathodic peak ($E_{reduction}$ = −0.75 V *vs.* RHE), and the cathodic current commenced to increase negatively from −0.15 V *vs.* RHE due to electrochemical conversion of species in the CO_2 NTP, in addition to HER. Simultaneously, we monitored the production rates of various gaseous and liquid products to assess the synergistic integration of CO_2 NTP with electrochemical CO_2 reduction, as depicted in Fig. 2(b). In the absence of CO_2 NTP, that is, with the plasma off (Fig. 2 (bi)), the system exhibited high selectivity for C1 gas products. Carbon monoxide is the predominant product, with its production rate reaching approximately 0.5 μmol s^{-1} cm^{-2} at −1.1 V. Hydrogen is the primary byproduct, with its rate increasing as the overpotential rises.

By changing the source and introducing CO_2 NTP DBD (*i.e.*, plasma activation or plasma on), we observed a shift in the reaction landscape/pathway. Although the CO production rate remained stable at approximately 0.13 μmol s^{-1} cm^{-2}, there was a notable increase in the C2 and C3 product yields. Ethylene emerged as the major C2 product, with a rate of 0.09 μmol s^{-1} cm^{-2}. Additionally, a diverse array of liquid oxygenates (acetate, ethanol, and propanol) and gaseous hydrocarbons (ethane and propylene) appeared, which were either absent or minimal under the plasma-off condition.

Voltage characteristics and reaction kinetics

To evaluate the performance of CuO under conditions pertinent to industrial applications, we conducted a series of

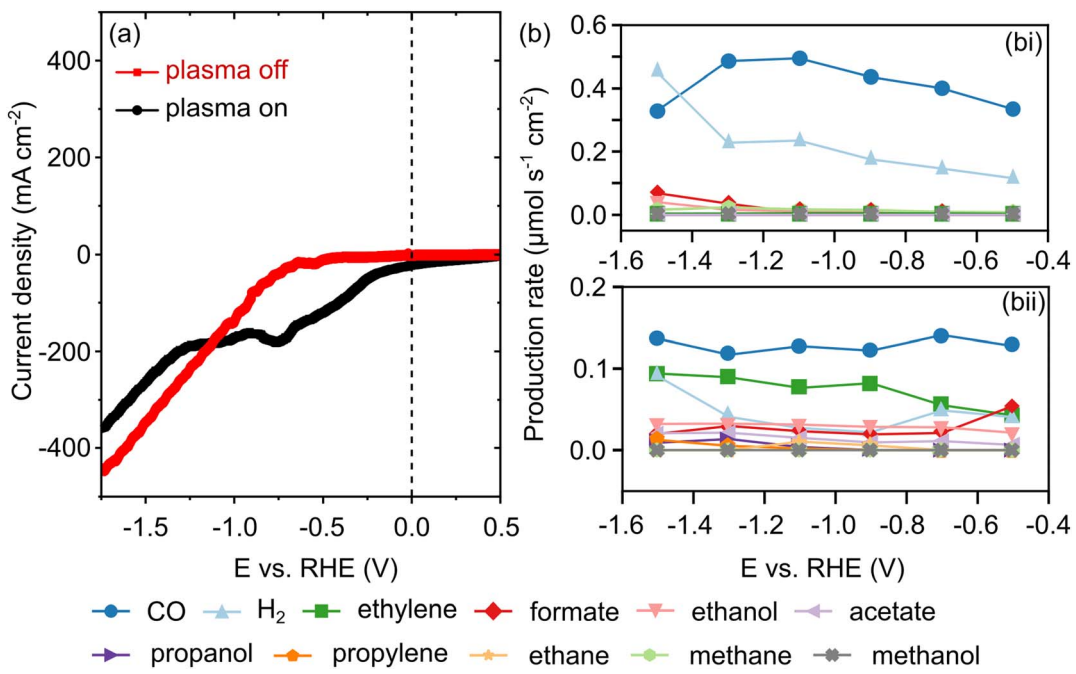

Fig. 2 Electrocatalytic performance and product selectivity transitions (a) LSV of CO_2 electrochemical conversion under two conditions: plasma-off (red line) and plasma-on (black line), scan rate = 50 mV s^{-1}. (b) Production rate of gas and liquid products *vs.* potential for (bi) electrochemical conversion with plasma-off and (bii) electrochemical conversion with plasma-on.

galvanostatic CO_2 reduction reaction (CO_2RR) experiments across a current density range of 100 to 225 mA cm^{-2}, Fig. S8–S13 and Table S2 (note Fig. S13 shows an image of the electrode after the electrolysis process). While fundamental laboratory studies frequently employ low current densities (<10 mA cm^{-2}) in H-cell configurations, achieving partial current densities exceeding 200 mA cm^{-2} is crucial for the techno-economic feasibility of CO_2 electrolysers.[58] By utilising a flow-cell architecture equipped with a GDE, we aimed to assess the influence of breaking the strong CO_2 bond by NTP. Galvanostatic control was specifically selected to maintain a constant production rate and to systematically investigate the evolution of the cell potential, which is sensitive to local pH fluctuations and the mechanical integrity of the triple-phase boundary at elevated reaction rates. Moreover, incremental step-wise testing from 100 to 225 mA cm^{-2} facilitated a precise mapping of the FE changes, providing critical insights into the onset of competitive HER and the durability of the GDE against flooding and carbonate precipitation.

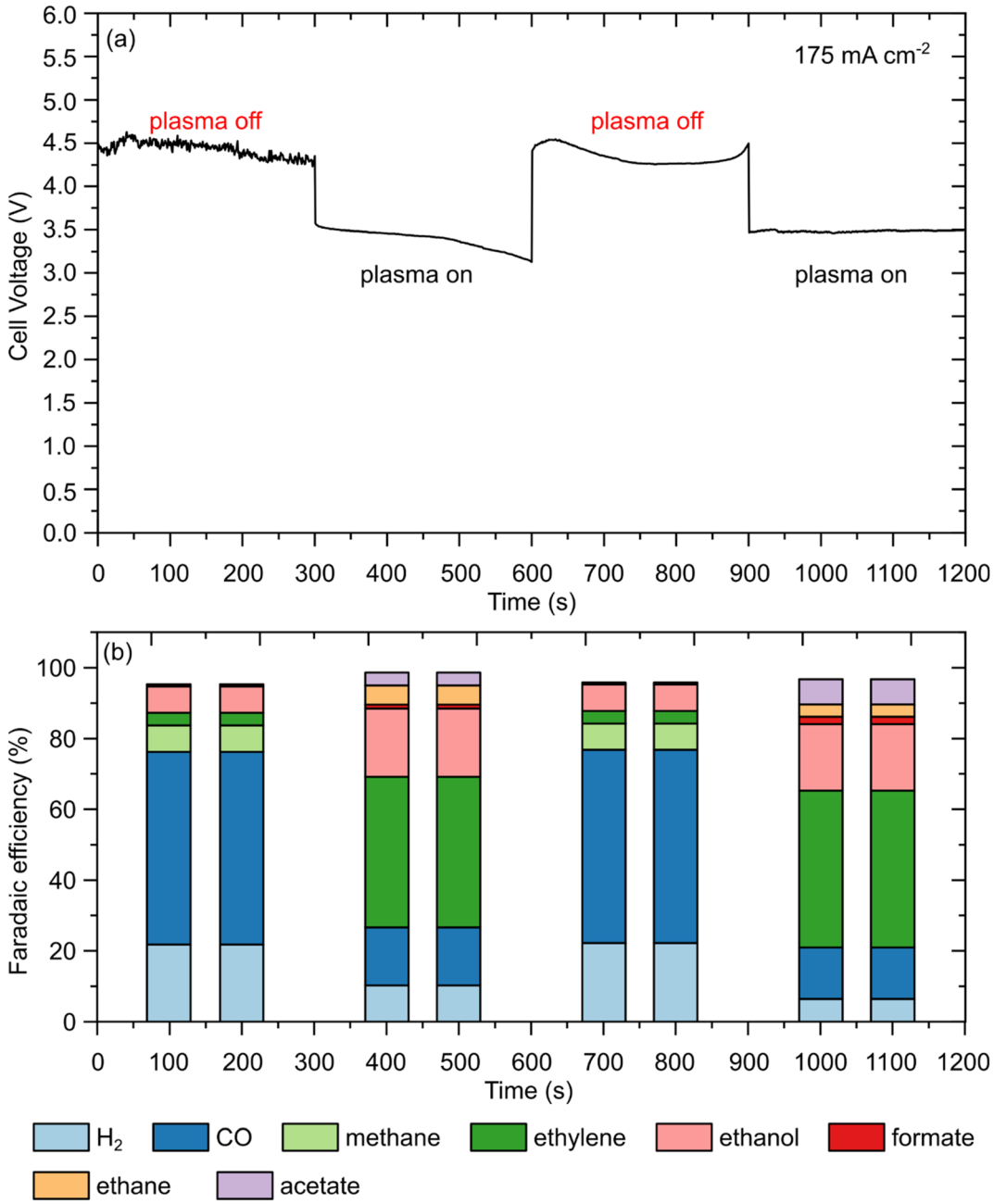

Fig. 3 Dynamic response of the electrolyte-gap electrolyser to plasma activation. (a) Chronopotentiogram profile at 175 mA cm^{-2} of CO_2 electrolysis using CO_2 gas and CO_2 NTP as reactant source, highlighting the voltage reduction (~1.0 V) upon switching from plasma-off to plasma-on conditions. Galvanostatic experiments were conducted in 0.5 M $CsHCO_3$ + 0.25 M $Cs(SO_3CH_3)$ + 0.25 M Cs_2SO_4 aqueous electrolyte. (b) Corresponding FE distribution of products obtained from CO_2 conversion reaction on CuO catalyst in the flow CO_2 electrolyser cell by switching between CO_2 NTP and CO_2 only at a current density of 175 mA cm^{-2}.

We investigated the effect of switching between plasma-off and plasma-on conditions, in which CO_2 gas was constantly fed into the electrolyte gap electrolyser, and the plasma power was turned on and off in real-time (Fig. 3). By operating the cell at a fixed current density of 175 mA cm^{-2}, the cell exhibited a high operational voltage of ~4.5 V during the plasma-off phase, and upon switching to the plasma-on mode, the cell voltage decreased significantly to ~3.5 V (Fig. 3(a)). The minor voltage drift observed during the initial plasma-on and subsequent plasma-off intervals is attributed to transient discharge stabilisation and the associated equilibration of gas transport and wetting; later segments approach a quasi-steady operational state. The transition to the plasma-on state significantly impacted the ethylene/carbon monoxide ratio and promoted the formation of liquid oxygenates (ethanol and acetate), as discussed below.

Under these conditions, as shown in Fig. 3(b), the FE during plasma-off was dominated by CO (FE 56.3%) and H_2 as a byproduct (FE 22.2%), with minor contributions from CH_4, C_2H_4, C_2H_5OH, and $HCOO^-$ (FEs of 5.1%, 3.2%, 8.7%, and 1%, respectively); see Fig. S5 and eqn (S1)–(S5) for FE calculations. Upon switching to the plasma-on mode, a distinct shift in the product distribution (Fig. 3(b)) was observed. Notably, methane production was suppressed below the detectable limit, while ethylene and acetate emerged with FEs of 4.8% and 3.2%, respectively. The activation of the plasma also markedly enhanced the selectivity toward C2 species; the FEs of ethane and ethanol increased to 40.5% and 20.1%, respectively, representing a substantial shift from CO-dominant to multicarbon-product-dominant electrocatalysis. Furthermore, the reduction in H_2 FE to 6.2% underscores the efficacy of the CO_2 NTP-electrochemical hybrid system in suppressing competitive HER and redirecting the electron flux toward high-value carbon products.

To decouple thermal effects from plasma-activated pathways, the impact of the feed gas temperature on cell voltage and product selectivity was evaluated (Fig. 4). Under the specific operating conditions ($P_{plasma} = 10 \pm 0.5$ W), the bulk temperature of the CO_2 NTP effluent was measured to be between 140–160 °C *via* external infrared thermometry.[59,60] This range represents an upper bound, as the external positioning of the high-voltage electrode and comparison with higher power regimes (>16 W) suggest the internal gas temperature is likely lower.[61] Notably, gas heating in DBD is highly sensitive to reactor geometry, power density, and flow dynamics; thus, these values are specific to this architecture.[60] Galvanostatic CO_2 RR was performed at a current density of 175 mA cm^{-2} for a duration of 1 hour to evaluate the influence of reactant activation modes. Three distinct experimental configurations were investigated: (1) ambient thermal control: plasma-off at 25 °C, (2) elevated thermal control: plasma-off at 150 °C (to simulate plasma-induced heating), and (3) plasma-activated: plasma-on utilising a CO_2 NTP DBD. The control experiment aimed to determine whether the product distribution observed during plasma-on operation stems from vibrationally or electronically excited CO_2 species rather than purely thermal effects.

To ensure a rigorous comparison of activation mechanisms, all experiments utilised identical electrolyte compositions, electrocatalysts, and ion-exchange membranes, thereby isolating the effects of reactant excitation from electrochemical cell variables. The performance of the electrolyte-gap electrolyser at a constant current density of 175 mA cm^{-2} is presented

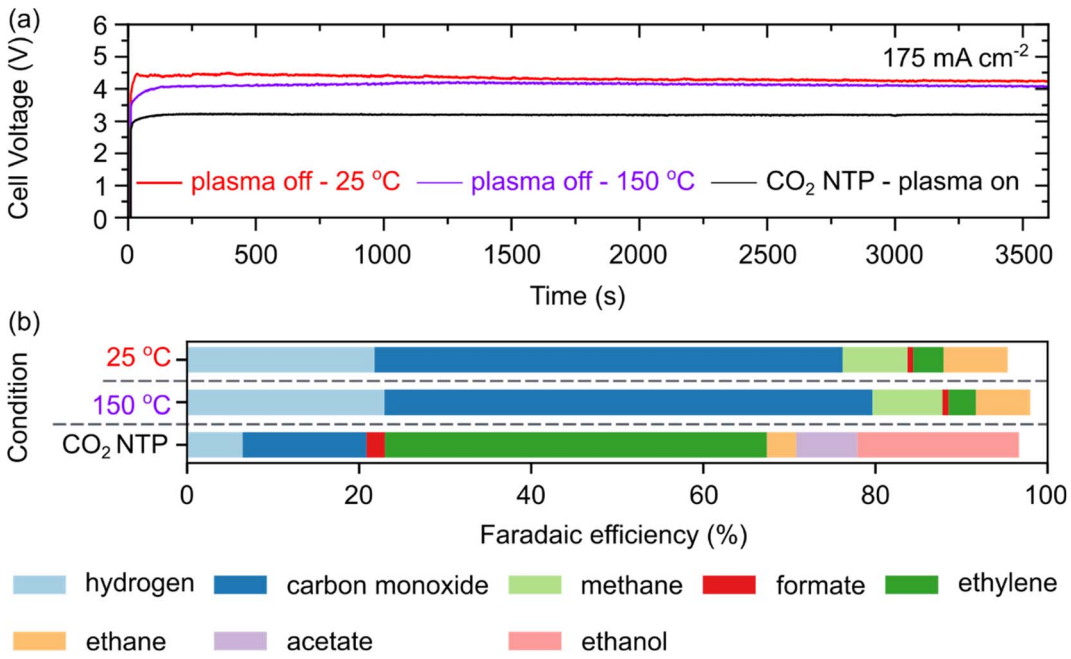

Fig. 4 Comparative performance of electrochemical CO_2 conversion under non-thermal, thermal, and plasma-activated conditions. Galvanostatic experiments were carried out at 175 mA cm^{-2} using the electrolyte-gap electrolyser and 0.5 M $CsHCO_3$ + 0.25 M $Cs(SO_3CH_3)$ + 0.25 M Cs_2SO_4 aqueous electrolyte. (a) Chronopotentiogram of CO_2 electrolysis using CO_2 gas at 25 °C (red line), 150 °C (purple line), and CO_2 NTP (black line) as the reactant source. (b) Corresponding FE of the products obtained.

in Fig. 4. Under plasma-off conditions at 25 °C, the cell voltage stabilised at 4.48 V following a brief induction period of approximately 1.5–2 s (Fig. 4(a), red trace). This was followed by a subtle, continuous decline to *ca.* 4.45 V over a 2600 s period. While temperature is known to influence CO_2 solubility, mass transport, and reaction thermodynamics,[21,62] our results show that increasing the CO_2 feed temperature from 25 °C to 150 °C (plasma-off) at a current density of 175 mA cm^{-2} resulted in only a negligible voltage decrease (from approximately 4.37 V at 25 °C to ~4.15 V at 150 °C, Fig. 4(a) purple line). In contrast, operation in plasma-on mode (Fig. 4 (a) black trace) resulted in a substantial reduction in cell voltage to 3.1 V. This potential remained highly stable throughout the 1 hour electrolysis period, representing a voltage saving of ~1.35 V compared to the conventional molecular CO_2 feed. The absence of significant voltage drift in the plasma-on mode suggests that the activation of the reactant feed may also assist in maintaining steady-state conditions at the electrode–electrolyte interface.

Furthermore, the product distribution resulting from ambient thermal control, that is, plasma-off at 25 °C and elevated thermal control, that is, plasma-off at 150 °C (comprising H_2, CO, CH_4, C_2H_4, C_2H_5OH, and $HCOO^-$), remained largely unchanged, with only a marginal increase in total FE by increasing the temperature of the CO_2 feed, as shown in Fig. 4(b). Conversely, we observed a transition toward C2 and C3 products upon integrating the CO_2 NTP DBD source with the electrochemical CO_2RR, as illustrated in Fig. 4(b).

The limited impact of preheating the CO_2 feed to 150 °C confirms that the enhancements observed during the plasma-on mode are not primarily driven by thermal energy. This highlights the non-thermal advantages of the plasma, in which energetic electrons and reactive species (*e.g.*, O^-, CO^+) facilitate CO_2 dissociation or stabilise intermediates for C–C coupling.[55,63] While OES confirmed the presence of radical species, a portion of the selectivity shift may arise from the modified feed composition (*i.e.*, CO/CO_2 mixtures generated *in situ*). Future studies utilising synthetic CO/CO_2/He blends are required to precisely quantify the synergy between non-thermal excited species and CO co-feeding.

To investigate the product distribution, the FE was monitored at 600 s intervals throughout the 1 hour electrolysis to assess the impact of reactant activation on product selectivity (Fig. 5). Notable shifts in the catalytic pathways were observed between the two operational modes. Under plasma-off conditions (Fig. 5(a)), the system predominantly produced C1 gaseous species, with carbon monoxide as the major product (FE = 54.6% ± 1.3), accompanied by methane (FE = 7.4% ± 0.76) and significant competitive HER (hydrogen FE = 26.1% ± 1.5). Small quantities of ethylene were also detected (FE = 3.55% ± 0.6). In contrast, the introduction of CO_2 NTP-DBD activation (Fig. 5(b)) fundamentally redirected the reaction toward C2+ pathways and suppressed the HER, with the hydrogen FE decreasing to 6.4% ± 1.25. Plasma-on operation promoted the formation of both gaseous and liquid multicarbon products. In the gaseous phase, we noticed significant enhancement in ethylene (FE = 44.31% ± 1.98) and the emergence of ethane (3.44% ± 0.57), while CO FE was reduced to 14.5% ± 1.4. From the liquid phase, we recorded the production of ethanol (18.83% ± 1.3), acetate (7.14% ± 0.65), and formate (2.15% ± 0.55). The transition from a C1 dominant regime to a combined gaseous/liquid C2+ distribution (total C2+ FE exceeding 70%) emphasises the advantage of plasma-assisted electrochemical CO_2 reduction. This selectivity shift is attributed to the presence of plasma-generated reactive species and vibrationally excited CO_2, which likely lower the kinetic barriers for carbon–carbon coupling and stabilise key surface intermediates, thereby bypassing conventional scaling relationships that typically limit C1 to C2+ conversion. The results accentuate the non-thermal nature of CO_2 plasma benefits, where energetic electrons and reactive species (*e.g.*, O^-, CO^+) directly participate in breaking CO_2 bonds or stabilising intermediates that facilitate C–C coupling,[56,63,64] potentially leading to non-explored CO_2 conversion pathways.

Despite the presence of high-energy electrons, ions, and reactive oxygen species (ROS) within the CO_2 NTP, the electrode showed no signs of significant delamination, sintering, or mechanical degradation, as shown in Fig. S13. The porous structure of the GDE, which is essential for efficient gas transport and maintenance of the triple-phase boundary, was preserved throughout the electrolysis period. Based on the experimental results, we drew the following observations regarding the electrode resilience. First, we discussed the thermal stability, in which the "non-thermal" nature, despite the involvement of high-energy species in the NTP, ensured that the bulk gas temperature remained relatively low, thereby preventing thermal damage to the PTFE binder or the carbon support within the GDE. Second, we tested the chemical robustness. Although the catalyst surface may undergo transient oxidation state changes (Cu^0 to $Cu^{\delta+}$) due to plasma-derived oxygen species, it did not exhibit irreversible poisoning or phase transformation that would inhibit CO_2 reduction kinetics. Third, we tested the catalyst adhesion, in which there was no evidence of catalyst "wash-off" into the catholyte, indicating that the plasma-on conditions did not compromise the interfacial bonding between the CuO nanoparticles and the gas diffusion layer. This demonstrated stability over one hour of continuous operation, suggesting that the plasma–electrochemical interface was robust enough for extended durability testing and potential scaling.

Galvanostatic electrochemical CO_2RR was performed at current densities (j) ranging from 100 to 225 mA cm^{-2} for 1 hour to evaluate the impact of plasma activation (plasma-on *vs.* plasma-off). Detailed results across the full current range are provided in the SI (Fig. S8–S12) and the corresponding cell voltage at each current density is shown in Fig. 6(a). Plasma-on operation consistently yielded lower cell voltages than plasma-off conditions across the entire current density range. For instance, at j = 100 mA cm^{-2}, the cell voltage decreased from 3.45 V (plasma-off) to 2.60 V (plasma-on), representing a potential reduction $|\Delta E| = E_{\text{plasma-off}} - E_{\text{plasma-on}} = 0.84$ V. This voltage gap widened significantly with increasing j, reaching a maximum difference of 2.03 V at 225 mA cm^{-2} ($E_{\text{plasma-off}}$ = 5.53 V *vs.* $E_{\text{plasma-on}}$ = 3.50 V). This substantial reduction in overpotential suggests that the introduction of reactive plasma-

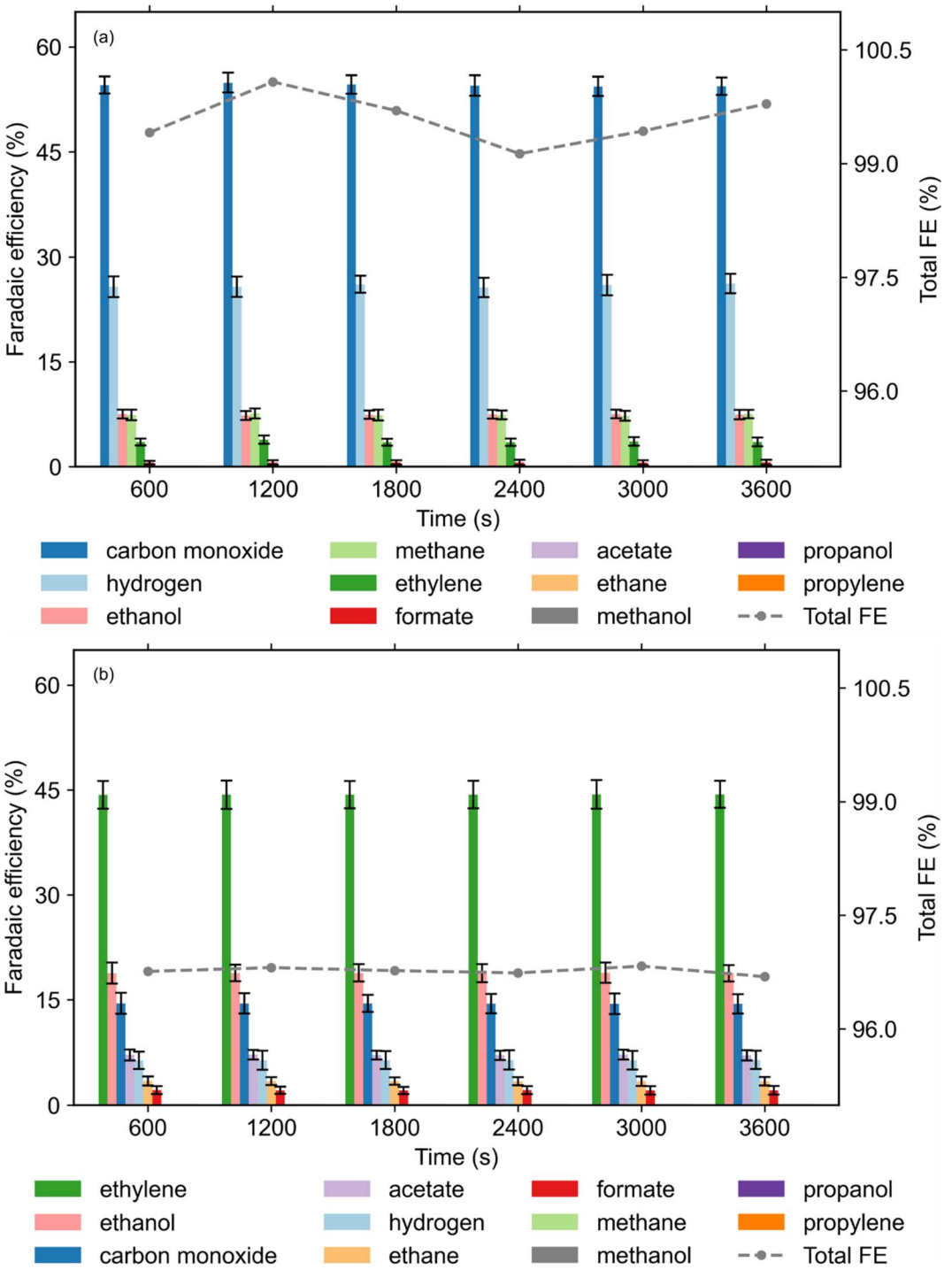

Fig. 5 Comparative FE for electrochemical CO_2 conversion at 175 mA cm^{-2} over 1 hour of electrolysis. (a) Product distribution under plasma-off conditions. (b) Product distribution under CO_2 NTP-DBD *i.e.* plasma-on conditions, demonstrates a strategic shift toward multicarbon gaseous and liquid products. Error bars represent the standard deviation ($n = 3$) calculated from GC and HPLC measurements sampled at 600 s intervals.

generated species lowers the kinetic barriers for charge transfer at the electrode–electrolyte interface.[65,66] The cumulative FE for C1–C3 species is illustrated in Fig. 6(b and c). The FE for C2 products (ethylene and ethanol) was maximised at lower current densities (100–150 mA cm^{-2}) under plasma-on conditions (Fig. 6(b and c)). Notably, the plasma-on mode facilitated the production of C3 species—specifically propylene and 1-propanol, which were absent during plasma-off experiments. While conventional electrochemical CO_2RR typically terminates at C2 intermediates,[67–69] the diversity of plasma-generated species (including CO molecules, ions, and excited-state intermediates) likely facilitates chain propagation. The emergence of propylene

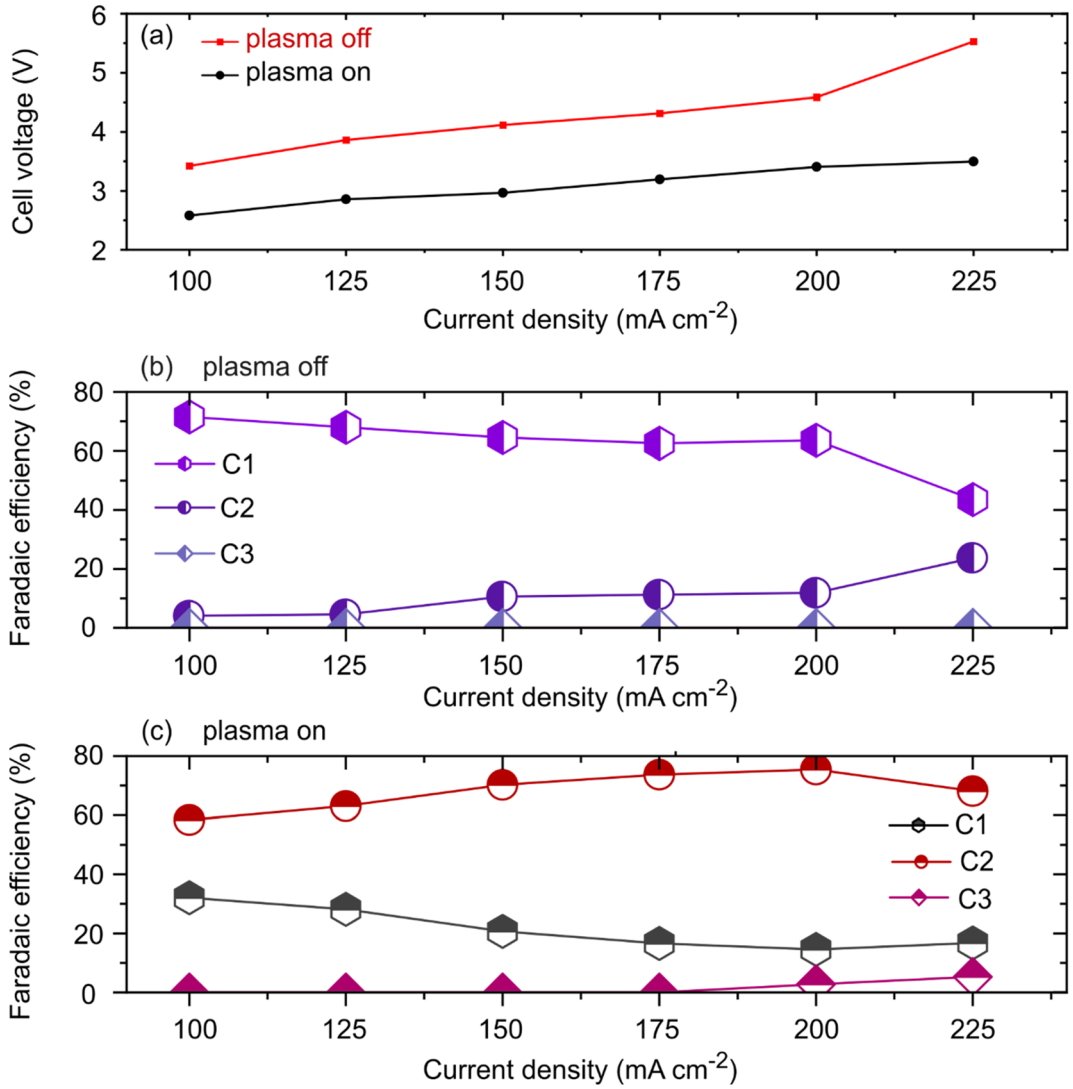

Fig. 6 Performance and selectivity of plasma-integrated electrochemical CO_2 reduction (a) cell voltage as a function of current density for plasma-off (red line) and plasma-on (black line) conditions across varying current densities (100–225 mA cm^{-2}). FE for gaseous products and liquid products (b) plasma-off and (c) plasma-on.

(FE ~3.95%) and 1-propanol at 200 mA cm^{-2} supports a plasma-mediated chain propagation mechanism.[67] It is hypothesised that the stabilisation of *CH_2 intermediates on asymmetric CuO sites promotes C–C coupling with *CO to form C3 precursors.[56,68,70] Comparative analysis highlights two critical advantages of plasma-integrated electrolysis: (1) enhanced cell voltage: the reactive nature of the plasma medium consistently lowers the operating cell voltage, a phenomenon attributed to the pre-activation of CO_2 molecules. (2) Product selectivity: plasma-on operation shifts the selectivity from primary syngas components (CO and H_2) toward high-value C2+ products. This is evidenced by the higher FE for ethylene and the unique synthesis of C3 hydrocarbons and alcohols, indicating a fundamental change in the reaction pathway mediated by plasma-generated intermediates.

The dependence of the gaseous and liquid product FE on j is summarised in Fig. 7(a–d). Under plasma-off conditions (Fig. 7(a and b)), CO was the primary gaseous product, although its FE declined from 64.74% at 100 mA cm^{-2} to 34.73% at 225 mA cm^{-2}. This downward trend in FE_{CO} was particularly pronounced at j > 150 mA cm^{-2}, correlating with increased competitive HER and the onset of liquid product formation. Specifically, ethanol and formate production commenced at 150 mA cm^{-2} (FE of 6.59% and 0.51%, respectively), with ethanol reaching a maximum FE of 22.12% at the highest current density. Methane production peaked at 200 mA cm^{-2} (FE = 8.85%), at which point ethylene selectivity was suppressed to its minimum (FE = 2.48%), suggesting a shift in intermediate pathways at high overpotentials.

Activation of the CO_2 plasma significantly diversified the product profile (Fig. 7(c and d)). The gas phase included ethane, ethylene, and propylene, whereas the liquid phase contained formate, acetate, ethanol, and 1-propanol. Notably, the introduction of plasma suppressed methane formation to non-

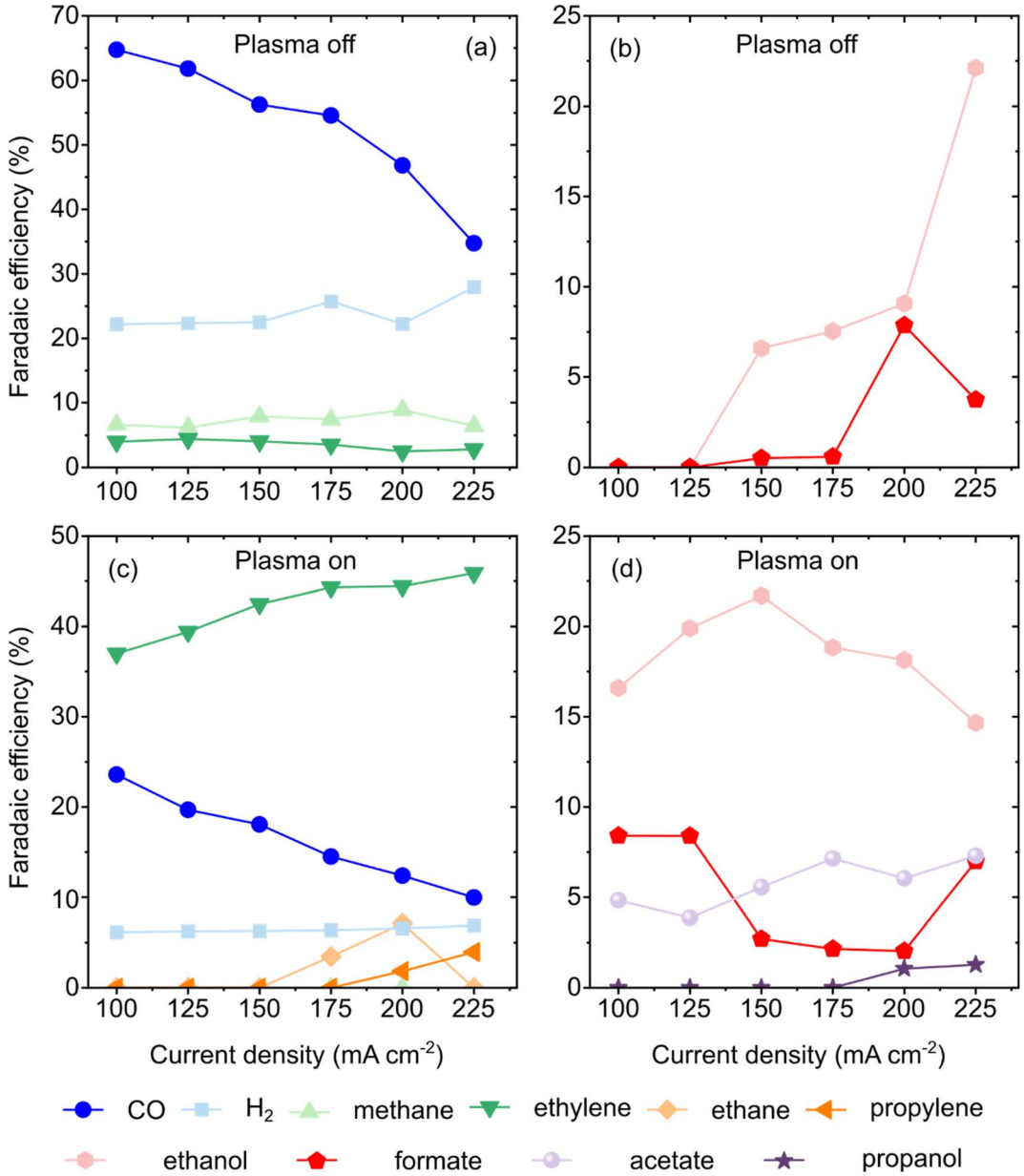

Fig. 7 Plasma-off (a and b) and plasma-on (c and d) FEs of CO_2 conversion to gas (a and c) and liquid (b and d) products as a function of the current density.

detectable levels and stabilised the FE of H_2 at an average of ~6.5%. Despite CO being the primary species generated within the CO_2 NTP,[50,52,71,72] its FE decreased as j increased. This was mirrored by a substantial increase in ethylene selectivity, which reached 45.89% at 225 mA cm^{-2}. This observation is consistent with the literature suggesting that plasma-generated CO serves as a high-concentration reactant that is more readily reduced to C2+ species than molecular CO_2.[73,74]

The plasma-on system uniquely facilitated the synthesis of C3 products. Propylene production was initiated at 200 mA cm^{-2}, reaching a maximum FE of 3.95% at 225 mA cm^{-2}. Similarly, 1-propanol was detected at higher current densities, peaking at 225 mA cm^{-2}, reaching an FE of 1.28%. In the liquid phase, ethanol remained the dominant product under plasma-on conditions, achieving a maximum FE of 21.69% at a relatively low current density of 150 mA cm^{-2}. The transition from formate (maximum FE 8.41% at 100 mA cm^{-2}) to acetate (maximum FE 7.29% at 225 mA cm^{-2}) further indicates that plasma-mediated species enhance C–C coupling by stabilising $*CH_2$ intermediates on asymmetric CuO sites and chain elongation pathways *via* $*CH_2$ intermediates that are inaccessible in conventional electrochemical systems.[35,75]

Assessing the energy efficiency (EE) of electrochemical CO_2RR, DBD NTP generation, and hybrid DBD-assisted CO_2 electrolysis is essential, as these electricity-driven processes exhibit distinct thermodynamic losses and downstream

requirements. For CO_2RR, performance benchmarking incorporates FE, j, and cell voltage into a comprehensive electrical-to-chemical efficiency metric ($EE = (FE \times \Delta V_{thermodynamic})/\Delta V_{cell}$). Techno-economic viability generally necessitates $j \geq 100-200$ mA cm^{-2} and EE $\geq$ 50%, with explicit reporting of carbon conversion efficiency to accurately reflect reactant utilisation.[58] The architecture of the reactor further influences these metrics; for example, GDE configurations in acidic media can enhance EE by ~30% relative to neutral electrolytes by mitigating carbonate-related penalties.[76] Conversely, the performance of DBD is determined by the specific energy input (SEI), which inherently involves a trade-off with CO_2 conversion (X_{CO_2}) and energy efficiency (η) *i.e.* the efficiency of utilising the plasma energy for the chemical conversion.[77] Exemplary values range from $\eta \approx 9.4\%$ at $X_{CO_2} \approx 4.2\%$ (SEI $\approx$ 25 kJ L^{-1}) to $\eta \approx 94.1\%$ at $X_{CO_2} \approx 51\%$ (SEI $\approx$ 155 kJ L^{-1}).[77]

The integration of CO_2 plasma with electrochemical CO_2 reduction significantly alters the product distribution and the EE across a range of current densities, as illustrated in Fig. 8, Fig. S14 and eqn (S6)–(S8). An EE_{CO} of 25.35% was achieved when the cell was operated under plasma-off conditions at a current density of 100 mA cm^{-2}. The EE_{CO} decreases with increasing current density, reaching a minimum value of 8.41% at a current density of 225 mA cm^{-2}. Methane was only produced under the plasma-off mode and reached a peak $EE_{methane}$ value of 2.85% at 100 mA cm^{-2} and a minimum $EE_{methane}$ value of 1.70% at 225 mA cm^{-2}. The $EE_{ethylene}$ gradually decreases with increasing current density, reaching a value of 1.84% at 100 mA cm^{-2} and a minimum of 0.8% at 225 mA cm^{-2}. This observation of the highest and lowest $EE_{methane}$ and $EE_{ethylene}$ values is associated with the production of liquid products, specifically formate and ethanol, where formate (C1 product) achieved the highest $EE_{formate}$ of 3.15% at 200 mA cm^{-2}, and ethanol (C2 product) the highest $EE_{ethanol}$ of 6.24% at 225 mA cm^{-2}. In general, under plasma-off conditions, the EE is predominantly concentrated in simpler products, with CO being the most significant. Methane and ethylene reached an EE between 0.5% and 3% across the applied current density range. Ethanol and formate were observed when current densities above 150 mA cm^{-2} were applied. This implies that, in the absence of plasma, the system favours C1 products (CO, CH_4) with limited formation of multi-carbon (C2) products (see also Fig. 6(b)).

As shown in Fig. 8(b), although plasma-on experiments lead to valuable C2+ products, this is at the expense of a much lower EE, both overall and for each product. EE_{CO} decreases with increasing current density, while $EE_{formate}$ first shows a high $EE_{formate}$ of 1.65% at 100 mA cm^{-2}, then decreases when the current is increased, and reaches a minimum $EE_{formate}$ of 0.24% at 200 mA cm^{-2}. This coincides with the emergence of various C2 and C3 products, mainly liquid C3 products. Despite this trend, $EE_{formate}$ increases when 225 mA cm^{-2} is applied and reaches 0.82%. $EE_{ethylene}$ shows a slight change during the investigated current densities (100–225 mA cm^{-2}), from $EE_{ethylene}$ of 0.51% at 100 mA cm^{-2} to $EE_{ethylene}$ of 0.48% at 225 mA cm^{-2}. $EE_{ethanol}$ exhibits a volcano trend with a maximum of 0.66% at 150 mA cm^{-2}, and EE_{ethane} reaches a maximum of 0.015% at 200 mA cm^{-2}. $EE_{acetate}$ presents an erratic response with current density, reaching a maximum of 0.51% at 175 mA cm^{-2}.

As sustained FE gains are achieved, $EE_{propylene}$ and $EE_{propanol}$ (C3 products produced solely under plasma-on conditions) increase with increasing current density. Both reached their

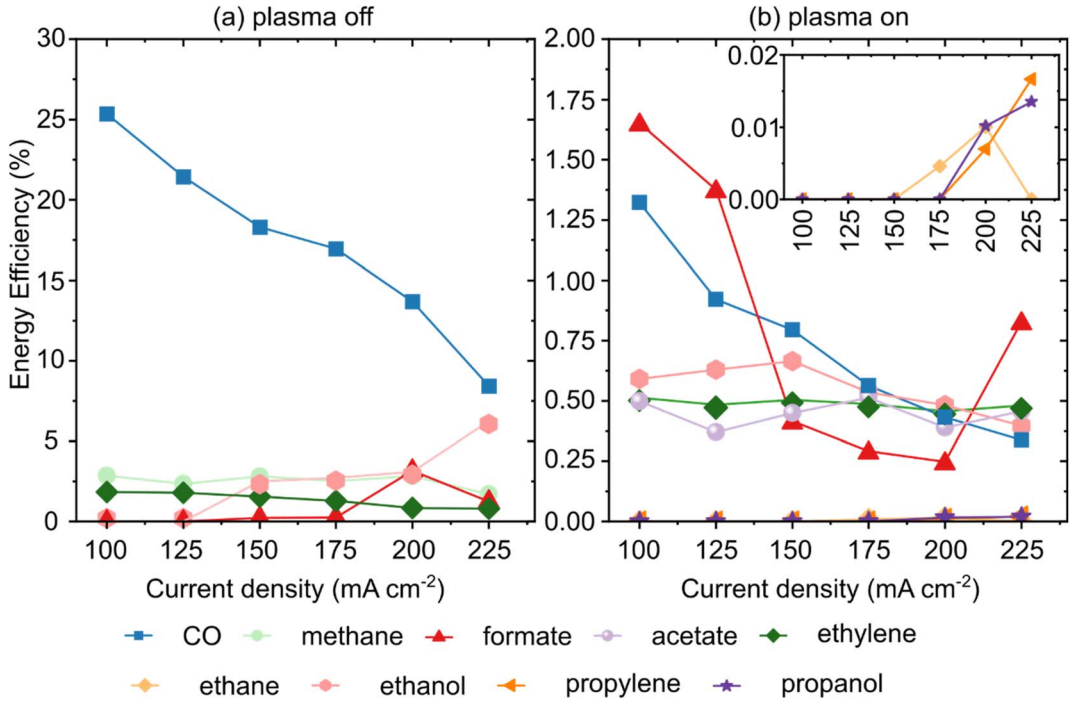

Fig. 8 (a) Plasma-off and (b) plasma-on energy efficiency for gases and liquid products *vs.* current density.

maximum EE values of 0.02% and 0.018%, respectively, at 225 mA cm^{-2}. The observed reduction in EE during plasma-on operation can be attributed to the incomplete coupling between the discharge and the catalytic interface. This is due to the separation of the discharge zone from the cathode by post-discharge transport, characterised by a rod tip-to-cathode distance of 10 mm. This separation and convection following discharge allow time for the plasma species to relax or recombine. CO and O recombine to form CO_2, resulting in a loss of conversion achieved within the plasma,[60,61] or return to the ground state through energy-relaxation processes before reaching the catalyst, an effect that is likely intensified by the presence of the GDE.[59,60] This results in the power deposited in the plasma not being utilised effectively, with the effect being variable depending on the lifetime of all plasma species.[59,60] Some of these, such as the radicals and vibrationally excited states, have relatively long lifetimes, whereas others, such as ions and electronically excited states, have much shorter lifetimes.[54,55,57,63,67,70,78] The species that reach the catalyst surface likely drive the conversion process. To enhance EE, it is anticipated that reducing post-discharge transport losses, such as by decreasing the discharge-to-GDE distance and minimising dead volume, optimising the flow rate to increase the proportion of activated species reaching the interface, and/or integrating the discharge closer to the GDE plane, will be necessary.

The analysis of carbon efficiency (%), as depicted in Fig. 9 and S6–S9, Tables S3–S8, evaluates the carbon yield (Y_{carbon}), which is defined as the percentage of the total CO_2 feed converted into detectable gaseous and liquid products. The carbon efficiency (%) or yield for the sum of gas, liquid, and carbonate products ranged from 1.86% to 2.47% under plasma-off conditions and from 1.33% to 2.45% under plasma-on conditions (Fig. S9 and Table S8). The remaining carbon yield predominantly consists of unreacted CO_2 (~75% plasma off and ~80% plasma on) exiting the gas stream. This may stem from GDE-based flow cells operating at high volumetric flow rates to mitigate mass transport limitations, and inorganic carbon species sequestered in the electrolyte. Plasma activation induces a distinct shift in carbon distribution. In the gas-phase and under plasma-off conditions, the gas-phase carbon efficiency is higher (1.71–2.12%) compared to plasma-on operation (0.91–1.52%) across the tested current densities (Table S3). This observation aligns with the predominant production of CO *via* the conventional $2e^-$ reduction pathway when the plasma is inactive. Conversely, in the liquid-phase, plasma activation significantly enhances liquid-phase carbon incorporation (Table S4). Notable production of C2 and C3 oxygenates (ethanol, propanol, acetate) were observed at low current densities (*e.g.*, 0.41% yield at 100 mA cm^{-2}), whereas liquid product formation was negligible under plasma-off conditions until 150 mA cm^{-2}. At 225 mA cm^{-2}, the reduction in gas-phase

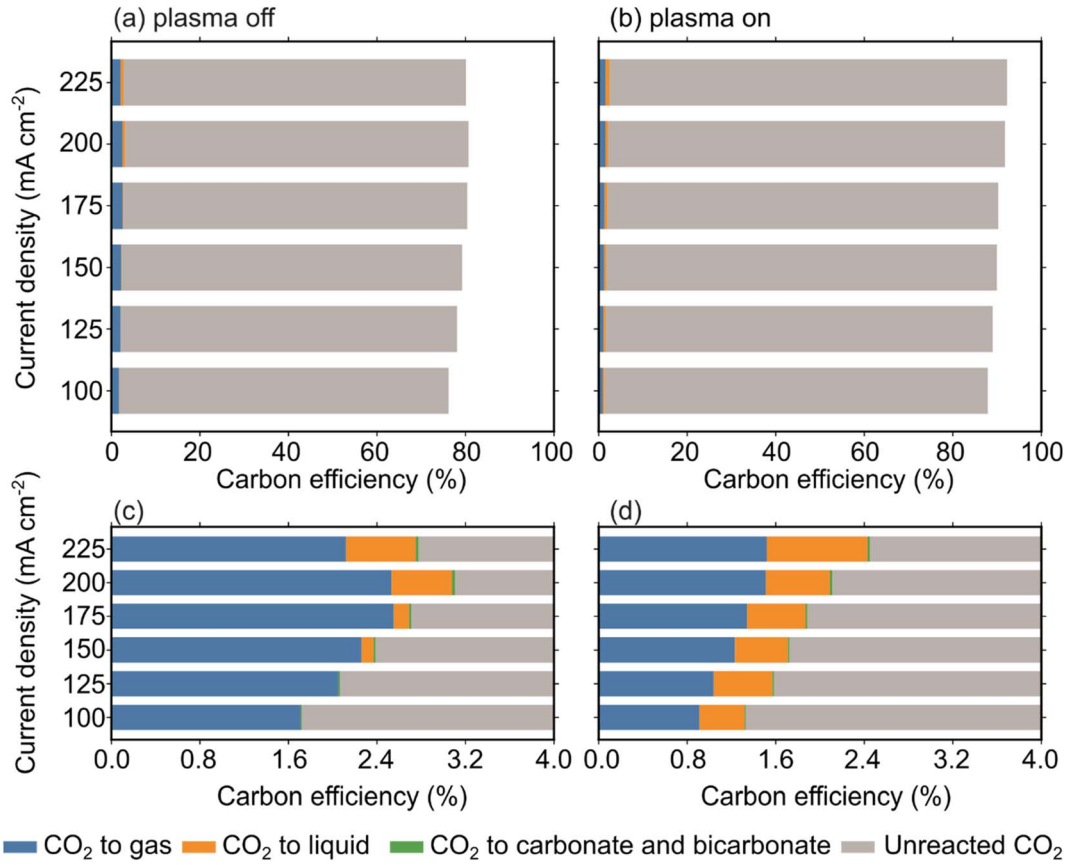

Fig. 9 Carbon efficiency (yield) for the conversion of CO_2 to gas, liquid, carbonate, and bicarbonate under (a and c) plasma off and (b and d) plasma on modes, (c and d) are zoom in plots.

yield under plasma-on conditions (1.52% *vs.* 2.12% for plasma-off) correlates with the diversion of carbon flux toward higher-order liquid products (liquid yield for plasma on is 0.91% *vs.* 0.63% for plasma off), confirming that plasma species facilitate chain growth over simple desorption as CO. In terms of inorganic carbon sequestration, we registered the formation of inorganic carbon byproducts (carbonate and bicarbonate) which act as a parasitic sink for the CO_2 feed. This sequestration was consistently higher under plasma-off conditions (0.011–0.027%) compared to plasma-on (0.01–0.022%). This difference is mechanistically linked to the interfacial pH environment. As detailed in Tables S6 and S7, plasma-off operation resulted in a highly alkaline effluent (pH 8.2–11.3), which shifts the equilibrium toward rapid CO_2 neutralisation:

$$CO_2 + 2OH^- \rightarrow CO_3^{2-} + H_2O.$$

This will result in increased crossover of carbon towards the anode and increased inorganic carbon reservoirs, such as membrane-stored carbonate, within the reactor. In contrast, the plasma-on mode maintained a more moderate pH (7.5–9.2), due to the formation of formate and acetate, which consume $n - 1$ protons per n electrons transferred. Consequently, plasma-on operation results in a smaller pH increase and less carbonate formation, thereby preserving a slightly larger fraction of the dissolved inorganic carbon for electrochemical conversion into high-value C2 and C3 fuels.

The results illustrate that plasma activation effectively suppresses HER, with the FE for H_2 decreasing from 22.2% (plasma-off) to 6.2% (plasma-on). This shift facilitates the redirection of the electron flux toward CO_2 reduction, thereby significantly enhancing the selectivity for C2 products. Specifically, the FE for ethylene increased from 3.2% to 40.5%, while ethanol production, undetectable under plasma-off conditions, reached an FE of 20.1%.

The CO_2 NTP DBD generates a diverse population of reactive species, including ions (CO_2^+, CO^+), molecules, excited states, radicals, and vibrationally or electronically excited states (CO_2^*, CO*).[38] The synergetic coupling of the CO_2 NTP DBD with electrochemical reduction induces a fundamental shift in both the energetic and kinetic landscapes of the reaction, beyond the substantial reduction in cell voltage. While CO and vibrationally excited CO_2 serve as primary reactive precursors for C2+ synthesis,[57,58,67,70,72,79] the concomitant generation of oxygen-bearing species (O, O_2, O_3) may play a role in the product distribution. These species potentially stabilise catalytic $Cu^{\delta+}$ moieties, known to promote C–C coupling by modifying CO adsorption energies,[6,34,35,66,67,80] although their reduction may simultaneously detract from overall EE. Collectively, these results suggest that the enhanced selectivity toward high-value C2+ products is a result of a multi-component synergy involving plasma-activated carbon species and transient oxygen-driven surface stabilisation of $Cu^{\delta+}$ species.

Interestingly, the plasma-on mode exhibits an attenuated local pH compared to plasma-off operation. This is attributed to the stoichiometric shift in product selectivity. The synthesis of carboxylates such as formate and acetate requires $n - 1$ protons per n transferred electrons, while all the other products (*e.g.* CO, methane, ethanol) consume the same number of electrons and protons. Consequently, the plasma-mediated pathway reduces the interfacial proton demand and leads to a smaller pH increase.

Notably, a reduction in cell voltage was observed during plasma-on operation, where an average decrease of ~1.3 V was attributed to two factors. First, the partial provision of the Gibbs free energy (ΔG) required for CO_2 reduction during the plasma excitation phase. Second, the emergence of alternative reaction pathways with lower activation energies ($E_{activation}$) for the reduction of plasma-activated species.

Mechanistically, the formation of propylene (FE 3.95%) alongside ethylene (FE 45.89%) suggests a coupling pathway between C2 intermediates and CO_2-derived radicals or carboxyl species (*COOH). At higher current densities (*e.g.*, 200 and 225 mA cm^{-2}), increased product diversity and C2 selectivity are observed, likely driven by a combination of plasma-induced kinetic enhancements and local mass transport dynamics. Additionally, the plasma-on state lowers the interfacial pH, thereby mitigating carbonate formation and directing the carbon flux toward liquid products, such as acetate and propanol.

The higher pH reached in the catholyte with plasma off facilitates the neutralisation of CO_2 by OH^-, resulting in the formation of HCO_3^-/CO_3^{2-}. This process consequently enhances (bi)carbonate formation and diminishes the proportion of carbon available for product synthesis.

Despite the shift toward value-added products, the sum of carbon efficiency for both gas and liquid remained low (average of 2.5% for plasma off *vs.* average of 2% for plasma on). These losses are attributed to CO_2 crossover, dissolution in the electrolyte, or adsorption within the GDE. Furthermore, while the electrochemical cell voltage decreases, the overall system EE remains low due to the energy-intensive nature of DBD NTP and subsequent recombination reactions (*e.g.*, $CO + O \rightarrow CO_2$) occurring in the post-discharge zone. Nevertheless, this hybrid system demonstrates the capability for flexible product tuning and provides a scalable framework for sustainable carbon utilisation.

Conclusions

We herein demonstrate a system that integrates a CO_2 DBD-NTP source with an electrolyte-gap CO_2 electrolyser utilising CuO-based cathodes, thereby facilitating a direct comparison between plasma-on and plasma-off operations at current densities of 100–225 mA cm^{-2}. Plasma-on operation consistently reduces the cell voltage and shifts product selectivity from C1-dominated products toward higher-value C2+ products, such as ethylene, propylene, formate, and acetate. Carbon analysis reveals that plasma-on operation redistributes carbon away from (bi)carbonate formation toward gas and liquid products; although the overall carbon recovery remains modest, indicating the presence of substantial unquantified sinks typical of GDE CO_2 electrolysis. Although the current configuration is not energy-efficient when accounting for plasma power, the findings establish a proof-of-concept for utilising plasma-activated feeds

to modulate CO_2RR selectivity within a flow-cell architecture. Future research will focus on enhancing the plasma–electrode coupling through optimisation of the geometry and residence time, and isolating the role of oxygen species.

Author contributions

H. E. M. H., P. N. K., and A. C. devised the concept of combined NTP-electrochemical platforms for CO_2 electrochemical conversion and designed a hybrid device. H. E. M. H. and P. N. K. performed the experiments. H. E. M. H. performed microscopy imaging. H. E. M. H. prepared the substrates and electrochemical device. H. E. M. H. and P. N. K. conducted the conversion experiments. H. E. M. H., P. N. K., and A. C. were involved in the data analysis. H. E. M. H., P. N. K. and A. C. wrote the manuscript.

Conflicts of interest

The authors declare no conflicts of interest.

Data availability

The data supporting this article are available at Zenodo (https://zenodo.org/records/19542797), DOI: 10.5281/zenodo.19542797.

Supplementary information (SI): tables of results, and figures S1–S9 (PDF). See DOI: https://doi.org/10.1039/d5se01488c.

Acknowledgements

This work is part of the Electrocatalysis in Non-Thermal Plasma for Energy Storage (COPLE) project funded by the Adventurous Energy Research for a Sustainable Net Zero Programme Grant from the EPSRC (EP/X000931/1). The authors thank Jonathan Boschen-Rose, Yaroslav Kruchek, Robert Skinner, Raymond Stephen, Jonathan Edwards, and Matthew Craib for their technical support.

References

1 S. Overa, B. H. Ko, Y. Zhao and F. Jiao, *Acc. Chem. Res.*, 2022, **55**, 638–648.
2 A. Dutta, M. Rahaman, M. Mohos, A. Zanetti and P. Broekmann, *ACS Catal.*, 2017, **7**, 5431–5437.
3 W. Choi, Y. Choi, E. Choi, H. Yun, W. Jung, W. H. Lee, H. S. Oh, D. H. Won, J. Na and Y. J. Hwang, *J. Mater. Chem. A*, 2022, **10**, 10363–10372.
4 M. Lima, C. M. Godoi, M. C. L. Santos, J. Nandenha, A. O. Neto and R. F. B. De Souza, *Int. J. Hydrogen Energy*, 2022, **47**, 4010–4017.
5 Y. Hori, I. Takahashi, O. Koga and N. Hoshi, *J. Phys. Chem. B*, 2002, **106**, 15–17.
6 M. Sassenburg, M. Kelly, S. Subramanian, W. A. Smith and T. Burdyny, *ACS Energy Lett.*, 2023, **8**, 321–331.
7 L. Hoof, N. Thissen, K. Pellumbi, K. junge Puring, D. Siegmund, A. K. Mechler and U.-P. Apfel, *Cell Rep. Phys. Sci.*, 2022, **3**, 100825.
8 A. Ozden, J. Li, S. Kandambeth, X. Y. Li, S. J. Liu, O. Shekhah, P. F. Ou, Y. Z. Finfrock, Y. K. Wang, T. Alkayyali, F. P. G. de Arquer, V. S. Kale, P. M. Bhatt, A. H. Ip, M. Eddaoudi, E. H. Sargent and D. Sinton, *Nat. Energy*, 2023, **8**, 179–190.
9 W. C. Ma, S. J. Xie, T. T. Liu, Q. Y. Fan, J. Y. Ye, F. F. Sun, Z. Jiang, Q. H. Zhang, J. Cheng and Y. Wang, *Nat. Catal.*, 2020, **3**, 478–487.
10 J. Schneider, H. Jia, J. T. Muckerman and E. Fujita, *Chem. Soc. Rev.*, 2012, **41**, 2036–2051.
11 S. Zhang, P. Kang, M. Bakir, A. M. Lapides, C. J. Dares and T. J. Meyer, *Proc. Natl. Acad. Sci. U. S. A.*, 2015, **112**, 15809–15814.
12 B. A. W. Mowbray, D. J. Dvorak, N. Taherimakhsousi and C. P. Berlinguette, *Energy Fuels*, 2021, **35**, 19178–19184.
13 K. Qi, Y. Zhang, N. Onofrio, E. Petit, X. Cui, J. Ma, J. Fan, H. Wu, W. Wang, J. Li, J. Liu, Y. Zhang, Y. Wang, G. Jia, J. Wu, L. Lajaunie, C. Salameh and D. Voiry, *Nat. Catal.*, 2023, **6**, 319–331.
14 G. Marcandalli, A. Goyal and M. T. M. Koper, *ACS Catal.*, 2021, **11**, 4936–4945.
15 M. Moura de Salles Pupo and R. Kortlever, *ChemPhysChem*, 2019, **20**, 2926–2935.
16 S. Garg, Q. C. Xu, A. B. Moss, M. Mirolo, W. Y. Deng, I. Chorkendorff, J. Drnec and B. Seger, *Energy Environ. Sci.*, 2023, **16**, 1631–1643.
17 Y. Zhao, L. Hao, A. Ozden, S. Liu, R. K. Miao, P. Ou, T. Alkayyali, S. Zhang, J. Ning, Y. Liang, Y. Xu, M. Fan, Y. Chen, J. E. Huang, K. Xie, J. Zhang, C. P. O'Brien, F. Li, E. H. Sargent and D. Sinton, *Nat. Synth.*, 2023, **2**, 403–412.
18 A. S. Varela, *Curr. Opin. Green Sustainable Chem.*, 2020, **26**, 100371.
19 X. Liu, P. Schlexer, J. Xiao, Y. Ji, L. Wang, R. B. Sandberg, M. Tang, K. S. Brown, H. Peng, S. Ringe, C. Hahn, T. F. Jaramillo, J. K. Nørskov and K. Chan, *Nat. Commun.*, 2019, **10**, 32.
20 M. C. O. Monteiro, A. Mirabal, L. Jacobse, K. Doblhoff-Dier, S. C. Barton and M. T. M. Koper, *JACS Au*, 2021, **1**, 1915–1924.
21 R. E. Vos, K. E. Kolmeijer, T. S. Jacobs, W. van der Stam, B. M. Weckhuysen and M. T. M. Koper, *ACS Catal.*, 2023, **13**, 8080–8091.
22 Y. Pei, H. Zhong and F. Jin, *Energy Sci. Eng.*, 2021, **9**, 1012–1032.
23 M. R. Gonçalves, A. Gomes, J. Condeço, R. Fernandes, T. Pardal, C. A. C. Sequeira and J. B. Branco, *Energy Convers. Manage.*, 2010, **51**, 30–32.
24 F.-Y. Gao, R.-C. Bao, M.-R. Gao and S.-H. Yu, *J. Mater. Chem. A*, 2020, **8**, 15458–15478.
25 D. R. Kauffman, J. Thakkar, R. Siva, C. Matranga, P. R. Ohodnicki, C. Zeng and R. Jin, *ACS Appl. Mater. Interfaces*, 2015, **7**, 15626–15632.
26 M. Zhong, K. Tran, Y. Min, C. Wang, Z. Wang, C.-T. Dinh, P. De Luna, Z. Yu, A. S. Rasouli, P. Brodersen, S. Sun, O. Voznyy, C.-S. Tan, M. Askerka, F. Che, M. Liu, A. Seifitokaldani, Y. Pang, S.-C. Lo, A. Ip, Z. Ulissi and E. H. Sargent, *Nature*, 2020, **581**, 178–183.

27 H. S. Jeon, S. Kunze, F. Scholten and B. Roldan Cuenya, *ACS Catal.*, 2018, **8**, 531–535.
28 H. Xu, D. Rebollar, H. He, L. Chong, Y. Liu, C. Liu, C.-J. Sun, T. Li, J. V. Muntean, R. E. Winans, D.-J. Liu and T. Xu, *Nat. Energy*, 2020, **5**, 623–632.
29 S. Nitopi, E. Bertheussen, S. B. Scott, X. Liu, A. K. Engstfeld, S. Horch, B. Seger, I. E. L. Stephens, K. Chan, C. Hahn, J. K. Norskov, T. F. Jaramillo and I. Chorkendorff, *Chem. Rev.*, 2019, **119**, 7610–7672.
30 S. Popovic, M. Bele and N. Hodnik, *ChemElectroChem*, 2021, **8**, 2634–2639.
31 S. Garg, M. R. Li, A. Z. Weber, L. Ge, L. Y. Li, V. Rudolph, G. X. Wang and T. E. Rufford, *J. Mater. Chem. A*, 2020, **8**, 1511–1544.
32 P. Ramadhany, Q. Luong, Z. Zhang, J. Leverett, P. Samorì, S. Corrie, E. Lovell, I. Canbulat and R. Daiyan, *Adv. Mater.*, 2024, **36**, 2405029.
33 D. Gao, R. M. Arán-Ais, H. S. Jeon and B. Roldan Cuenya, *Nat. Catal.*, 2019, **2**, 198–210.
34 S. You, J. Xiao, S. Liang, W. Xie, T. Zhang, M. Li, Z. Zhong, Q. Wang and H. He, *Energy Environ. Sci.*, 2024, **17**, 5795–5818.
35 B. Chang, H. Pang, F. Raziq, S. Wang, K.-W. Huang, J. Ye and H. Zhang, *Energy Environ. Sci.*, 2023, **16**, 4714–4758.
36 J. Gao, A. Bahmanpour, O. Kröcher, S. M. Zakeeruddin, D. Ren and M. Grätzel, *Nat. Chem.*, 2023, **15**, 705–713.
37 S. Kumari, S. Pishgar, M. E. Schwarting, W. F. Paxton and J. M. Spurgeon, *Chem. Commun.*, 2018, **54**, 13347–13350.
38 S. Mori and L. L. Tun, *Plasma Processes Polym.*, 2017, **14**, 1600153.
39 S. Ringe, E. L. Clark, J. Resasco, A. Walton, B. Seger, A. T. Bell and K. Chan, *Energy Environ. Sci.*, 2019, **12**, 3001–3014.
40 B. Huang, K. H. Myint, Y. Wang, Y. Zhang, R. R. Rao, J. Sun, S. Muy, Y. Katayama, J. Corchado Garcia, D. Fraggedakis, J. C. Grossman, M. Z. Bazant, K. Xu, A. P. Willard and Y. Shao-Horn, *J. Phys. Chem. C*, 2021, **125**, 4397–4411.
41 M. C. O. Monteiro, F. Dattila, B. Hagedoorn, R. García-Muelas, N. López and M. T. M. Koper, *Nat. Catal.*, 2021, **4**, 654–662.
42 G. Marcandalli, M. C. O. Monteiro, A. Goyal and M. T. M. Koper, *Acc. Chem. Res.*, 2022, **55**, 1900–1911.
43 A. Xu, N. Govindarajan, G. Kastlunger, S. Vijay and K. Chan, *Acc. Chem. Res.*, 2022, **55**, 495–503.
44 J. C. Bui, C. Kim, A. J. King, O. Romiluyi, A. Kusoglu, A. Z. Weber and A. T. Bell, *Acc. Chem. Res.*, 2022, **55**, 484–494.
45 M. R. Singh, Y. Kwon, Y. Lum, J. W. Ager, III and A. T. Bell, *J. Am. Chem. Soc.*, 2016, **138**, 13006–13012.
46 M. Gattrell, N. Gupta and A. Co, *J. Electroanal. Chem.*, 2006, **594**, 1–19.
47 O. Ayemoba and A. Cuesta, *ACS Appl. Mater. Interfaces*, 2017, **9**, 27377–27382.
48 Q. Wu and Z. J. Xu, *Angew. Chem., Int. Ed.*, 2025, **64**, e202505022.
49 J. M. Yoo, J. Ingenmey, M. Salanne and M. R. Lukatskaya, *J. Am. Chem. Soc.*, 2024, **146**, 31768–31777.
50 D. H. Mei and X. Tu, *J. CO2 Util.*, 2017, **19**, 68–78.
51 H. Chen, Y. Mu, Y. Shao, S. Chansai, S. Xu, C. E. Stere, H. Xiang, R. Zhang, Y. Jiao, C. Hardacre and X. Fan, *Catal. Sci. Technol.*, 2019, **9**, 4135–4145.
52 C. Charalambous, S. Xu, S. Ding, S. Chansai, E. Asuquo, A. Torres Lopez, C. M. A. Parlett, J. D. Gilmour, A. Garforth and C. Hardacre, *Front. Chem. Eng.*, 2022, **4**, 1027167.
53 C.-j. Liu, G.-h. Xu and T. Wang, *Fuel Process. Technol.*, 1999, **58**, 119–134.
54 S. S. Xu, H. H. Chen, C. Hardacre and X. L. Fan, *J. Phys. D Appl. Phys.*, 2021, **54**, 233001.
55 C. Mas-Peiro, H. Quinteros-Lama, J. O. Pou and F. Llovell, *J. Chem. Eng. Data*, 2023, **68**, 1376–1387.
56 S. Xu, H. Chen, C. Hardacre and X. Fan, *J. Phys. D: Appl. Phys.*, 2021, **54**, 233001.
57 A. Mukhtar, S. Saqib, D. Mohotti, R. Ndeddy Aka, Jr., M. Hossain, E. Agyekum-Oduro and S. Wu, *Environ. Sci. Pollut. Res.*, 2025, **32**, 27314–27334.
58 D. Wakerley, S. Lamaison, J. Wicks, A. Clemens, J. Feaster, D. Corral, S. A. Jaffer, A. Sarkar, M. Fontecave, E. B. Duoss, S. Baker, E. H. Sargent, T. F. Jaramillo and C. Hahn, *Nat. Energy*, 2022, **7**, 130–143.
59 R. Snoeckx and A. Bogaerts, *Chem. Soc. Rev.*, 2017, **46**, 5805–5863.
60 A. Bogaerts, A. Berthelot, S. Heijkers, S. Kolev, R. Snoeckx, S. Sun, G. Trenchev, K. Van Laer and W. Wang, *Plasma Sources Sci. Technol.*, 2017, **26**, 063001.
61 G. Centi, S. Perathoner and G. Papanikolaou, *J. CO2 Util.*, 2021, **54**, 101775.
62 R. E. Vos, J. P. Smaak and M. T. M. Koper, *J. Catal.*, 2024, **436**, 115613.
63 A. George, B. Shen, M. Craven, Y. Wang, D. Kang, C. Wu and X. Tu, *Renew. Sustain. Energy Rev.*, 2021, **135**, 109702.
64 M.-Y. Song, H. Cho, G. P. Karwasz, V. Kokoouline and J. Tennyson, *J. Phys. Chem. Ref. Data*, 2024, **53**, 033102.
65 K. R. Rasmi, S. C. Vanithakumari, R. P. George and U. Kamachi Mudali, *J. Mater. Eng. Perform.*, 2014, **23**, 1673–1679.
66 T. Yan, X. Chen, L. Kumari, J. Lin, M. Li, Q. Fan, H. Chi, T. J. Meyer, S. Zhang and X. Ma, *Chem. Rev.*, 2023, **123**, 10530–10583.
67 J. Hu and F. Liu, *Adv. Energy Sustain. Res.*, 2025, **6**, 2400339.
68 F. Wang, B. Wang, T. Zhang and J. Liu, *Green Carbon*, 2025.
69 M. Dauda, J. Hendershot, M. Bello, J. Park, A. Loaiza Orduz, N. Lombardo, O. Kizilkaya, P. Sprunger, A. Engler, C. Plaisance and J. Flake, *J. Electrochem. Soc.*, 2024, **171**, 034501.
70 J. Simon and L. R. Winter, *Curr. Opin. Green Sustainable Chem.*, 2025, **51**, 100985.
71 C. De Bie, J. van Dijk and A. Bogaerts, *J. Phys. Chem. C*, 2016, **120**, 25210–25224.
72 C. C. Jen, J. H. Hsieh and W. Wu, *IEEE Trans. Plasma Sci.*, 2024, **52**, 2948–2958.
73 N. S. Romero Cuellar, K. Wiesner-Fleischer, M. Fleischer, A. Rucki and O. Hinrichsen, *Electrochim. Acta*, 2019, **307**, 164–175.
74 B. Ruqia, G. M. Tomboc, T. Kwon, J. Kundu, J. Y. Kim, K. Lee and S.-I. Choi, *Chem Catal.*, 2022, **2**, 1961–1988.

75 M. Choi, S. Bae, Y. Kim, Y. Lee, M. Cho, S. Kang and J. Lee, *Nat. Catal.*, 2025, **8**, 476–486.
76 G. O. Larrazábal, A. J. Martín and J. Pérez-Ramírez, *J. Phys. Chem. Lett.*, 2017, **8**, 3933–3944.
77 T. Nozaki, X. Chen, D.-Y. Kim and C. Zhan, *Plasma Chem. Plasma Process.*, 2023, **43**, 1385–1410.
78 L. Liu, J. Dai, Z. Yang, Y. Li, X. Su and Z. Zhang, *Chem. Eng. J.*, 2022, **431**, 134009.
79 J. Wan, H. Zhang, J. Zheng, B. Lan, Y. Gang, Q. Huang and X. Li, *Carbon Capture Sci. Technol.*, 2024, **11**, 100197.
80 Y. Yao, T. Shi, W. Chen, J. Wu, Y. Fan, Y. Liu, L. Cao and Z. Chen, *Nat. Commun.*, 2024, **15**, 1257.